

Nonlinear Hall effect in two-dimensional class AI metals

Zi-Shan Liao,¹ Hong-Hao Zhang,¹ and Zhongbo Yan^{1,*}

¹*School of Physics, Sun Yat-Sen University, Guangzhou 510275, China*

(Dated: April 20, 2021)

In a time-reversal invariant system, while the anomalous Hall effect identically vanishes in the linear response regime due to the constraint of time-reversal symmetry on the distribution of Berry curvature, a nonlinear Hall effect can emerge in the second-order response regime if the inversion symmetry is broken to allow a nonzero Berry curvature dipole (BCD) on the Fermi surface. In this work, we study the nonlinear Hall effect of the BCD origin in two-dimensional doped insulators and semimetals belonging to the symmetry class AI which has spinless time-reversal symmetry. Despite that the class AI does not host any strong topological insulator phase in two dimensions, we find that they can still be classified as topologically obstructed insulators and trivial insulators if putting certain constraint on the Hamiltonians. When the insulator gets closer to the phase boundary of the two distinct phases, we find that the BCDs will become more prominent if the doping level is located near the band edge. Moreover, when the insulator undergoes a phase transition between the two distinct phases, we find that the BCDs will dramatically change their signs. For the semimetals without inversion symmetry, we find that the BCDs will sharply reverse their signs when the doping level crosses the Dirac points. With the shift of the locations of Dirac points in energy, the critical doping level at which the BCDs sharply reverse their signs will accordingly change. Our study reveals that class AI materials can also have interesting geometrical and topological properties, and remarkable nonlinear Hall effect can also appear in this class of materials even though the spin-orbit coupling is negligible. Our findings broaden the scope of materials to study the nonlinear Hall effect and provide new perspectives for the application of this effect.

I. INTRODUCTION

In the past few decades, the study of topological phases has revealed that both symmetry and topology have strong impact on the response of materials to external fields [1]. One celebrated example is the anomalous Hall effect (AHE) contributed by Berry curvature [2]. In the linear response regime, it is known that the AHE identically vanishes in a time-reversal invariant system, owing to the constraint of time-reversal symmetry on the distribution of Berry curvature [3]. On the other hand, the AHE will be robustly quantized in a two-dimensional time-reversal broken insulator if the topological invariant, the net Chern number of its occupied bands, is nonzero [4–6]. In physics, such robust quantized responses are appealing since their robustness allows interesting applications [7], meanwhile, they provide an experimentally accessible and faithful way to extract the underlying topological property of the concerned system. However, quantized responses are commonly restricted to topological gapped systems and, being certain discrete quantities, can only reflect the global topological property and its discrete change. As the local quantum geometry of the Bloch wave functions, like Berry curvature, contains much richer information than its global counterpart, known as the topological invariant, and it can have nontrivial distribution even in a topologically trivial system, non-quantized responses related to the local quantum geometry can appear in much more materials and can extract more information about the band structure of the concerned system.

In recent years, it has been shown that several kinds of nonlinear electromagnetic responses, including injection current photogalvanic effect [8–10], shift current photogalvanic effect [8, 11–15], nonlinear Hall effect [16, 17] and so on, have a

close connection to the local quantum geometry in momentum space [18–20]. Remarkably, the nonlinear Hall effect reveals that a Hall-like current can occur in time-reversal invariant and inversion breaking systems as a second-order response to external electric fields [16, 17]. Being a second-order intraband effect, the Hall-like current is found to have a close connection with the dipole moment of the Berry curvature in momentum space, the so-called Berry curvature dipole (BCD) [17]. Mathematically, the BCD is an integral of the product of local Berry curvature and velocity over the Fermi surface, so metals with prominent Berry curvature near the Fermi surface are ideal platforms to observe this effect. Under this guiding principle, as band degeneracies are natural sources of divergent Berry curvature, three-dimensional Weyl semimetals [21–30], two-dimensional transition-metal dichalcogenides [31–41], strained graphene [42–44] and topological insulators close to the phase boundary [45], which have either tilted gapless Weyl cones or tilted gapped Dirac cones, have been actively studied both theoretically and experimentally [46, 47]. As the nonlinear Hall effect is an effect related to Fermi surface, it is noteworthy that doping is necessary for its observation in pristine gapped systems, such as topological insulators.

By far, most of works have focused on systems with sizable spin-orbit coupling, with only a few exceptions [42, 48]. When the spin-orbit coupling plays a important role in the band structure, the spin degrees of freedom must be taken into account and the time-reversal symmetry operator satisfies $\mathcal{T}^2 = -1$. In the ten-fold way classification, it is known that the spinful time-reversal symmetry allows the existence of strong topological insulators in two and three dimensions [49–51]. In contrast, when the spin-orbit coupling is negligible, the spin degrees of freedom can be neglected and the time-reversal symmetry becomes its spinless counterpart following $\mathcal{T}^2 = 1$. When only the spinless time-reversal symmetry is

present, it is known that the system belongs to the symmetry class AI in the ten-fold way classification. It is worth noting that the class AI does not support any strong topological insulator phase (“strong” means that the gapless boundary states are robust against symmetry-preserving perturbations and do not depend on which direction is chosen to be open) in one, two and three dimensions [49–51], implying the absence of class AI strong topological insulators in real materials. Because of this absence, materials belonging to the class AI have attracted much less interest from the topological aspect. Accordingly, the geometrical and topological properties of the band structures as well as the related electromagnetic responses in this class of materials have been poorly explored.

In this work, we consider both insulators and semimetals belonging to the class AI in two dimensions and investigate, under different doping levels, how the nonlinear Hall effect responds to the change of quantum geometry and topology in band structures. For the class AI insulators in two dimensions, Although there is no strong topological phase, we find that they can still be classified as topologically obstructed insulators and trivial insulators if putting certain constraint on the Hamiltonians. The remarkable distinctions between these two kinds of phases are manifested in whether there exist boundary-direction-sensitive edge states and the distinct patterns of hybrid Wannier centers. Near the critical points between these two distinct phases, we find that the BCDs near the band edge will become more prominent when the system gets closer to the critical points. Notably, when going across the critical points, the BCDs will dramatically reverse their signs. For the semimetals, the topological properties and the locations of Dirac points (DPs) are of particular interest. In this work, we consider the Mielke model in which the DPs can move along the Brillouin zone boundary and merge, accompanying with the change in quantum geometry and topology [52, 53]. As the Berry curvature is divergent at the DPs, we find that the BCDs will sharply reverse their signs when the doping level crosses the DPs. With the shift of locations of DPs in momentum and energy, the critical doping level at which the BCDs sharply reverse their signs will accordingly change. For both insulators and semimetals, the results suggest that the nonlinear Hall effect can be quite remarkable in materials with negligible spin-orbit coupling and is sensitive to the change in quantum geometry and topology.

The structure of the paper is as follows. In Sec. II, we investigate the constraint put by the time-reversal symmetry and inversion symmetry on the class AI models and briefly review the nonlinear Hall effect. In Sec. III, we consider two representative models realizing class AI insulators and study the evolution of BCDs with respect to the change of band topology. In Sec. IV, we take the Mielke model as a representative example to study the evolution of nonlinear Hall effect with respect to the movement and mergence of DPs. We conclude with a detailed discussion in Sec. V.

II. THEORETICAL FORMALISM

As the spinless time-reversal symmetry does not enforce Kramers degeneracy at any momentum, and the nonlinear Hall effect is an effect related to Fermi surface, it is a good starting point to consider two-band class AI Hamiltonians. It is known that an arbitrary two-band Hamiltonian, in terms of the Pauli matrices, can be expanded as

$$\mathcal{H}(\mathbf{k}) = \sum_{i=0,x,y,z} d_i(\mathbf{k}) \sigma_i. \quad (1)$$

Here we assume that the Pauli matrices σ_i act on two orbital or sublattice degrees of freedom. Without the loss of generality, we further assume that under the given basis, the operator for the spinless time-reversal symmetry is simply the complex conjugate operator \mathcal{K} , i.e. $\mathcal{T} = \mathcal{K}$. Accordingly, $\mathcal{T}^2 = 1$ is followed, and the spinless time-reversal symmetry forces $\mathcal{H}^*(\mathbf{k}) = \mathcal{H}(-\mathbf{k})$, or equivalently, $d_{0,x,z}(\mathbf{k}) = d_{0,x,z}(-\mathbf{k})$, and $d_y(-\mathbf{k}) = -d_y(\mathbf{k})$.

The energy spectra of the Hamiltonian in Eq.(1) read

$$E_{\pm}(\mathbf{k}) = d_0(\mathbf{k}) \pm \sqrt{d_x^2(\mathbf{k}) + d_y^2(\mathbf{k}) + d_z^2(\mathbf{k})}. \quad (2)$$

For the above spectra, it is easy to see that the existence of band degeneracy requires the three components $\{d_x, d_y, d_z\}$ to vanish simultaneously at the same momentum. When the dimension $D \geq 3$, stable band degeneracies can exist as the number of momentum variables is equal to or larger than the number of constraint equations to fulfill. In contrast, the band degeneracy can only be accidental in one and two dimensions if there is no additional symmetry to force certain components of $\{d_x, d_y, d_z\}$ to vanish.

Besides the time-reversal symmetry, the inversion symmetry also puts strong constraints on the Hamiltonian. When the Hamiltonian has inversion symmetry, it needs to obey the constrain $\mathcal{P}\mathcal{H}(\mathbf{k})\mathcal{P}^{-1} = \mathcal{H}(-\mathbf{k})$ with \mathcal{P} a unitary matrix satisfying $\mathcal{P}^2 = 1$. As the time-reversal operator and inversion operator commute, \mathcal{P} has three possible choices for the given Hamiltonian in Eq.(1), i.e. $\mathcal{P} = \sigma_0, \sigma_x$ or σ_z . If $\mathcal{P} = \sigma_0$, then the inversion symmetry forces $d_{0,x,y,z}(\mathbf{k}) = d_{0,x,y,z}(-\mathbf{k})$. In combination with the time-reversal symmetry, one immediately finds that $d_y(\mathbf{k})$ identically vanishes throughout the Brillouin zone. If $\mathcal{P} = \sigma_x(\sigma_z)$, then $d_{0,x}(\mathbf{k}) = d_{0,x}(-\mathbf{k})$ and $d_{y,z}(-\mathbf{k}) = -d_{y,z}(\mathbf{k})$ ($d_{0,z}(\mathbf{k}) = d_{0,z}(-\mathbf{k})$ and $d_{x,y}(-\mathbf{k}) = -d_{x,y}(\mathbf{k})$), which indicates that $d_z(\mathbf{k})$ ($d_x(\mathbf{k})$) identically vanishes. In other words, when both time-reversal symmetry and inversion symmetry are present, one of the three components $\{d_x, d_y, d_z\}$ is forced to vanish identically, consequently allowing the presence of stable point band degeneracies in two dimensions. A celebrated example is the existence of Dirac points in graphene[54].

For the two-band Hamiltonian in Eq.(1), the Berry curvature has a simple expression, which reads [55]

$$\Omega_a^{(\pm)}(\mathbf{k}) = \pm \epsilon_{abc} \frac{\mathbf{d}(\mathbf{k}) \cdot (\partial_b \mathbf{d}(\mathbf{k}) \times \partial_c \mathbf{d}(\mathbf{k}))}{4d^3(\mathbf{k})}, \quad (3)$$

where the subscripts \pm refer to the conduction and valence bands, respectively, ϵ_{abc} is the third-rank Levi-Civita symbol, $\mathbf{d}(\mathbf{k}) = (d_x(\mathbf{k}), d_y(\mathbf{k}), d_z(\mathbf{k}))$, $d(\mathbf{k}) = |\mathbf{d}(\mathbf{k})|$, and $\partial_a \equiv \frac{\partial}{\partial k_a}$. In Eq.(3), we have assumed the summation over the repeated indices. As is known, the time-reversal symmetry forces $\Omega_a^{(\pm)}(\mathbf{k}) = -\Omega_a^{(\pm)}(-\mathbf{k})$ and the inversion symmetry forces $\Omega_a^{(\pm)}(\mathbf{k}) = \Omega_a^{(\pm)}(-\mathbf{k})$ [3]. These two properties can also be simply inferred through the symmetry constraints on $d_{x,y,z}$ discussed previously. Apparently, the coexistence of these two symmetries forces the Berry curvature to vanish identically in momentum space as long as there is no band degeneracy at which the Berry curvature is singular (note the denominator in Eq.(3) vanishes at the band degeneracy). These symmetry constraints indicate that in a time-reversal invariant system, the inversion symmetry must be broken to observe effects induced by Berry curvature.

It is known that a nonzero Berry curvature will contribute an anomalous velocity in the semiclassical equations of motion [3], consequently, applying an electric field is possible to generate a transverse Hall current even in the absence of an external magnetic field, which is known as the anomalous Hall effect. In the linear response regime, the generated Hall current j_α and the applied electric field \mathcal{E}_b are connected by the Hall conductivity σ_{ab} , i.e. $j_\alpha = \sigma_{ab}\mathcal{E}_b$, where σ_{ab} is an antisymmetric tensor satisfying $\sigma_{ab} = -\sigma_{ba}$. The general formula for σ_{ab} takes the form (we take $\hbar = 1$ throughout this paper)

$$\sigma_{ab} = e^2 \epsilon_{abc} \int \frac{d^D k}{(2\pi)^D} \sum_\alpha f^{(\alpha)}(\mathbf{k}) \Omega_c^{(\alpha)}(\mathbf{k}), \quad (4)$$

where α runs over all bands and $f^{(\alpha)}(\mathbf{k}) = 1/(1 + \exp(E_\alpha(\mathbf{k}) - \mu)/k_B T)$ is the Fermi-Dirac distribution function for the α th band, with μ denoting the chemical potential, k_B the Boltzmann constant and T the temperature. When the spinless time-reversal symmetry is conserved, $E_\alpha(\mathbf{k}) = E_\alpha(-\mathbf{k})$ and $\Omega_c^{(\alpha)}(-\mathbf{k}) = -\Omega_c^{(\alpha)}(\mathbf{k})$. Apparently, the integrand in Eq.(4) is an odd function of momentum, so σ_{ab} is forced to vanish, indicating the absence of Hall current in a time-reversal invariant system when restricting to the linear response regime.

Remarkably, the constraint on Hall current by the time-reversal symmetry can be lifted when taking into account higher-order responses. Using the semiclassical equations of motion, Sodemann and Fu derived that a dc as well as a second-harmonic Hall-like current can appear in the second-order response regime, as long as the inversion symmetry is broken [17]. Under an oscillating electric field $\mathbf{E} = \text{Re}\{\mathcal{E}e^{i\omega t}\}$ with the amplitude vector \mathcal{E} and frequency ω , the full Hall-like current can be written compactly as $j_a = \text{Re}\{j_a^{(0)} + j_a^{(2)}e^{2i\omega t}\}$, where $j_a^{(0)} = \chi_{abc}\mathcal{E}_b\mathcal{E}_c^*$ describes the dc part, and $j_a^{(2)} = \chi_{abc}\mathcal{E}_b\mathcal{E}_c$ describes the second-harmonic part. Interestingly, the coefficients in the two parts are equal and take the form [17]

$$\chi_{abc} = -\frac{e^3 \tau}{2(1 + i\omega\tau)} \epsilon_{adc} D_{bd}, \quad (5)$$

where τ denotes the relaxation time which is assumed to be a constant, and D_{bd} is the BCD which takes the form

$$\begin{aligned} D_{bd} &= -\sum_\alpha \int \frac{d^D k}{(2\pi)^D} \partial_b f^{(\alpha)}(\mathbf{k}) \Omega_d^{(\alpha)}(\mathbf{k}) \\ &= \sum_\alpha \int \frac{d^D k}{(2\pi)^D} f^{(\alpha)}(\mathbf{k}) \partial_b \Omega_d^{(\alpha)}(\mathbf{k}). \end{aligned} \quad (6)$$

The first line contains a factor $\partial_b f^{(\alpha)}$, which is equal to $-\partial_b E_\alpha \delta(\mu - E_\alpha)$ at the zero-temperature limit. The formula indicates that the BCD is an integral of the product of Berry curvature and Fermi velocity over the Fermi surface.

It is worth noting that the Berry curvature has only one component in two dimensions, namely $\Omega_z(\mathbf{k})$. As the second label of D_{bd} is fixed in this dimension, we will follow Ref. [17] and adopt the shorthand notation D_x and D_y to substitute D_{xz} and D_{yz} for a simplification of the notation.

III. NONLINEAR HALL EFFECT IN DOPED CLASS AI INSULATORS

A. Insulators with low-energy linear Dirac cones

Now let us focus on concrete class AI models and explore their geometrical and topological properties, as well as the nonlinear Hall effect. As the first representative example, we consider that the four components of d_i take the following form,

$$\begin{aligned} d_0(\mathbf{k}) &= t_0 \sin k_x \sin k_y, \\ d_x(\mathbf{k}) &= t_1 \cos k_y, \quad d_y(\mathbf{k}) = t_2 \sin k_x, \\ d_z(\mathbf{k}) &= (m + t_3 \cos k_x + t_4 \cos k_y). \end{aligned} \quad (7)$$

For notational simplicity, the lattice constants are set to unity throughout this paper. Through dimensional analysis, it is easy to find that the BCD is of the dimension of length in two dimensions, so the full expression for BCD can be simply restored by multiplying the dimensionless BCD with the corresponding lattice constant in real materials. As $d_{0,x,z}(\mathbf{k}) = d_{0,x,z}(-\mathbf{k})$, and $d_y(-\mathbf{k}) = -d_y(\mathbf{k})$, the Hamiltonian has the spinless time-reversal symmetry, but the inversion symmetry is broken according to our previous analysis. When $t_0 = 0$, the Hamiltonian has one additional mirror symmetry, i.e. $\mathcal{M}_y \mathcal{H}(k_x, k_y) \mathcal{M}_y^{-1} = \mathcal{H}(k_x, -k_y)$ with $\mathcal{M}_y = \sigma_0$. The mirror symmetry \mathcal{M}_y will force the Berry curvature to be odd in k_y , i.e. $\Omega_z^{(\pm)}(k_x, k_y) = -\Omega_z^{(\pm)}(k_x, -k_y)$. As the time-reversal symmetry forces $\Omega_z^{(\pm)}(-k_x, -k_y) = -\Omega_z^{(\pm)}(k_x, k_y)$, a combination leads to $\Omega_z^{(\pm)}(k_x, k_y) = \Omega_z^{(\pm)}(-k_x, k_y)$. Because the Fermi distribution function $f^{(\pm)}(k_x, k_y)$ is also an even function of k_x when $t_0 = 0$, one can easily infer from Eq.(6) that D_x is identically equal to zero for this case. According to Eq.(5), $D_x = 0$ implies $\chi_{yxx} = \chi_{xxy} = 0$. For linearly polarized light, $\chi_{yxx} = 0$ implies that the Hall-like current is absent when the electric vector is in the x direction. This result can also be intuitively understood by noting that

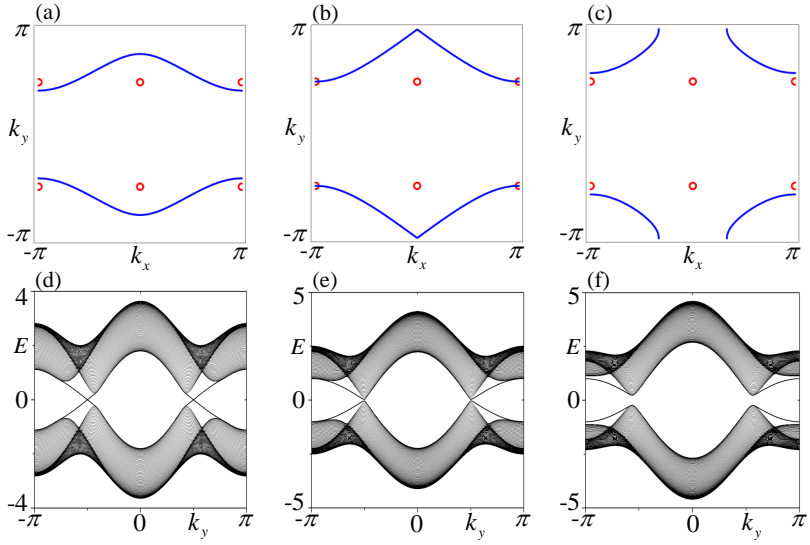


FIG. 1. (Color online) (a)-(c) Configurations of BIS (blue lines) and DPs (red points) in the bulk Brillouin zone. (d)-(e) Energy spectra for a cylinder geometry with open boundary conditions in the x direction and periodic boundary conditions in the y direction. Common parameters are $t_0 = 0$, $t_1 = t_3 = 1$ and $t_2 = t_4 = 2$. $m = 0.5$ in (a)(d), $m = 1$ in (b)(e), and $m = 1.5$ in (c)(f).

under the mirror reflection \mathcal{M}_y , the current and electric field follow the change: $\{j_x, j_y; \mathcal{E}_x, \mathcal{E}_y\} \rightarrow \{j_x, -j_y; \mathcal{E}_x, -\mathcal{E}_y\}$. Accordingly, the existence of mirror symmetry \mathcal{M}_y implies $j_y = \chi_{yxx}\mathcal{E}_x\mathcal{E}_x = -j_y$ and $j_x = \chi_{xxy}\mathcal{E}_x\mathcal{E}_y = -\chi_{xxy}\mathcal{E}_x\mathcal{E}_y$, so $\chi_{yxx} = \chi_{xxy} = 0$. When $t_0 \neq 0$, because the d_0 term does not affect the Berry curvature, the relation $\Omega_z^{(\pm)}(k_x, k_y) = \Omega_z^{(\pm)}(-k_x, k_y)$ remains hold. However, the Fermi distribution function $f^{(\pm)}(k_x, k_y)$ is no longer invariant under $k_x \rightarrow -k_x$, so a finite D_x becomes possible.

Before calculating D_x and D_y , we first explore the geometrical and topological properties of the Hamiltonian. As none of the three components $\{d_x, d_y, d_z\}$ vanishes identically, the Hamiltonian in general has a gapped spectra and thus describes an insulator. Despite that the Hamiltonian, according to the ten-fold way classification, cannot realize strong topological phases whose gapless boundary states are insensitive to the orientation of boundary, it can be still topologically nontrivial in a general sense. That is, in some regimes, the Hamiltonian, if putting certain constraint, cannot be adiabatically deformed to the trivial atomic limit without the closing of bulk gap. In such obstructed regimes, the Hamiltonian can still harbor gapless edge states on some boundary and meanwhile the hybrid Wannier centers of its bands also display nontrivial features.

We first provide an intuitive bulk picture for the existence of obstructed regime. For the convenience of discussion, we term the contour satisfying $d_z(\mathbf{k}) = 0$ as band inversion surface (BIS), and the points simultaneously satisfying $d_x(\mathbf{k}) = d_y(\mathbf{k}) = 0$ as Dirac points (DPs). As long as the BIS can be adiabatically deformed to vanish without closing the bulk gap, the phase is adiabatically connected to the atomic limit ($m \rightarrow \infty$) and is thus topologically trivial, otherwise the

system falls into the obstructed regime.

The quantum anomalous Hall insulator with inversion symmetry can be taken as the simplest realization of topologically obstructed phase. Let us take the Qi-Wu-Zhang model for illustration, where $d_x = \sin k_y$, $d_y = -\sin k_x$, and $d_z(\mathbf{k}) = c(2 - \cos k_x - \cos k_y - e_s)$ [55]. For this inversion symmetric model, the DPs satisfying $d_x(\mathbf{k}) = d_y(\mathbf{k}) = 0$ are pinned at the four time-reversal invariant momenta. When the BIS satisfying $d_z(\mathbf{k}) = 0$ encloses one of the DPs, i.e. $0 < |e_s| < 2$ with $c \neq 0$, it is easy to see that, because of the periodicity of Brillouin zone, the BIS cannot be adiabatically deformed to vanish without crossing the DPs (the bulk gap gets closed when they cross), so such a situation corresponds to the obstructed regime. For the Qi-Wu-Zhang model, it is apparent that the four unmovable DPs at the time-reversal invariant momenta are essential for the obstruction.

For the Hamiltonian in Eq.(7), it is readily found that there are also four DPs. However, they are not located at the time-reversal invariant momenta. Instead, they are located at $(k_x, k_y) = (0, \pm\pi/2)$ and $(\pi, \pm\pi/2)$ in the first Brillouin zone. As these four DPs are not pinned at the four special time-reversal invariant momenta, they are in principle movable and can annihilate. For instance, one can add a symmetry-preserving term of the form $\delta\sigma_x$ to the Hamiltonian in Eq.(7), then the DPs will annihilate and disappear when $|\delta| > |t_1|$. The absence of unremovable DPs can be taken as the underlying reason why the class AI does not host strong topological phase in two dimensions. For real materials, however, if the DPs are there, their positions may be quite stable under the change of certain experimental conditions, such as the pressure. With this in mind, here we will make an assumption that the DPs, though their locations are not at

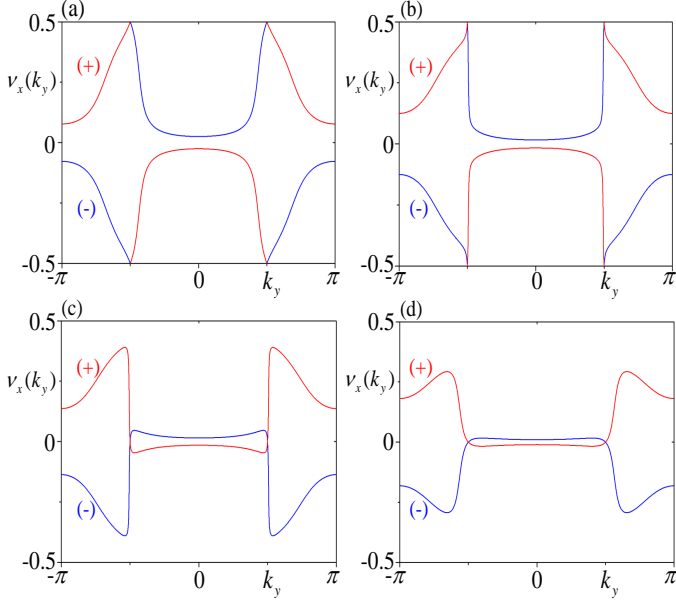


FIG. 2. (Color online) The hybrid Wannier centers $\nu_x^\pm(k_y)$. (a) $m = 0.5$, (b) $m = 0.95$, (c) $m = 1.05$, (d) $m = 1.5$. The hybrid Wannier centers undergo a dramatic change in structure when m crosses the critical point at $m = 1$. Common parameters are $t_0 = 0$, $t_1 = t_3 = 1$ and $t_2 = t_4 = 2$.

the time-reversal invariant momenta, are fixed in momentum space, and only the BIS changes. Under this assumption, the class AI insulators can also be classified as topologically obstructed insulators and trivial insulators according to the configurations of BIS and DPs.

Without the loss of generality, in the following we take $t_1 = t_3 = 1$ and $t_2 = t_4 = 2$ for a concrete discussion. For this set of parameters, $-1 < m < 1$ is found to be the obstructed regime of the Hamiltonian in Eq.(7). To see this in an intuitive way, we show the BIS and DPs together in the first Brillouin zone. The result for $m = 0.5$ is shown in Fig.1(a). It is readily found that under this parameter condition, the BIS (blue lines) cannot be continuously deformed to vanish without crossing the fixed DPs (red points). As the bulk gap gets closed when the BIS and DPs cross, it means that if starting with $m = 0.5$, the BIS cannot be adiabatically deformed to vanish without closing the bulk gap, so it corresponds to the obstructed regime. At $m = 1$, the crossing of BIS and DPs shown in Fig.1(b) indicates that the bulk gap is closed at this critical point. The result for $m = 1.5$ is shown in Fig.1(c). It is readily found that under this parameter condition, the BIS can be continuously deformed to vanish without closing the bulk gap, indicating that the Hamiltonian now falls into the trivial regime.

Now we consider a cylinder geometry with open boundary conditions in the x direction and periodic boundary conditions in the y direction and show the corresponding energy spectra under the same parameter conditions as in Figs.1(a)-(c). According to the results in Fig.1(d)-(f), it is readily found that

the Hamiltonian harbors gapless edge states only in the obstructed regime. It is worth noting that if the boundary conditions are reversed, namely open boundary conditions in the y direction and periodic boundary conditions in the x direction, then gapless edge states are always absent (so not shown explicitly), regardless of whether the Hamiltonian is in the obstructed regime or not. This is consistent with the fact that the Hamiltonian cannot realize a strong topological phase for which the existence of gapless edge states does not depend on the choice of boundary.

In the following, we further show the hybrid Wannier centers which are determined by calculating the corresponding Wilson loop. For the two-band Hamiltonian in Eq.(7), the Wilson loops in the x and y directions have the form [56]

$$W_x^{(\pm)}(k_y) = \prod_{n=0}^{N_x-1} \langle u^{(\pm)}(\mathbf{k}_{n,x}) | u^{(\pm)}(\mathbf{k}_{n+1,x}) \rangle,$$

$$W_y^{(\pm)}(k_x) = \prod_{n=0}^{N_y-1} \langle u^{(\pm)}(\mathbf{k}_{n,y}) | u^{(\pm)}(\mathbf{k}_{n+1,y}) \rangle,$$

where $\mathbf{k}_{n,x} = \mathbf{k} + n\Delta\mathbf{k}_x$ with $\Delta\mathbf{k}_x = (2\pi/N_x, 0)$ and $\mathbf{k}_{n,y} = \mathbf{k} + n\Delta\mathbf{k}_y$ with $\Delta\mathbf{k}_y = (0, 2\pi/N_y)$, $|u^\pm(\mathbf{k})\rangle$ denote the wave functions of the upper and lower bands, respectively, and $|u^\pm(\mathbf{k})\rangle$ obey the periodic gauge, i.e. $|u^\pm(\mathbf{k})\rangle = |u^\pm(\mathbf{k} + \mathbf{G})\rangle$ with \mathbf{G} the reciprocal lattice vector. Based on the Wilson loops, the hybrid Wannier centers are given by [56]

$$\nu_x^{(\pm)}(k_y) = -\frac{1}{2\pi} \text{Im} \ln W_x(k_y),$$

$$\nu_y^{(\pm)}(k_x) = -\frac{1}{2\pi} \text{Im} \ln W_y(k_x), \quad (8)$$

where Im denotes to take the imaginary part. As $\nu_x^{(\pm)}$ and $\nu_y^{(\pm)}$ are gauge-invariant modulo 1, in this work we choose the domain $\nu_{x,y}^{(\pm)} \in (-0.5, 0.5]$. Because the $d_0(\mathbf{k})$ term does not affect the wave functions, we find that the mirror symmetry \mathcal{M}_y forces $\nu_y^{(\pm)}(k_x)$ to take the trivial zero value for arbitrary k_x , which is consistent with the absence of gapless excitations on the y -normal edges. The numerical results for $\nu_x^{(\pm)}(k_y)$ are shown in Figs.2(a)-(d). It is readily seen that $\nu_x^{(\pm)}(k_y)$ display remarkable difference in the obstructed regime and trivial regime. In the obstructed regime, $\nu_x^{(\pm)}(k_y)$ will always cross the domain boundary $\nu = 0.5$ (this value corresponds to a π Berry phase as the Berry phase $\phi = 2\pi\nu$ at $k_y = \pm\pi/2$). In contrast, in the trivial regime, $\nu_x^{(\pm)}(k_y)$ cross the domain center $\nu = 0$ at $k_y = \pm\pi/2$. Here the reason for the crossings to be fixed at $k_y = \pm\pi/2$ is simply because the DPs satisfying $d_x(\mathbf{k}) = d_y(\mathbf{k}) = 0$ are fixed at $(k_x, k_y) = (0, \pm\pi/2)$ and $(\pi, \pm\pi/2)$.

As the Hamiltonian has a dramatic change in geometrical and topological properties when going from the obstructed regime to the trivial regime, it is interesting to investigate how the nonlinear Hall effect responds to this change. To make D_x nonzero, we consider t_0 to be finite. Besides the breaking of mirror symmetry, here another effect of the t_0 term is tilting

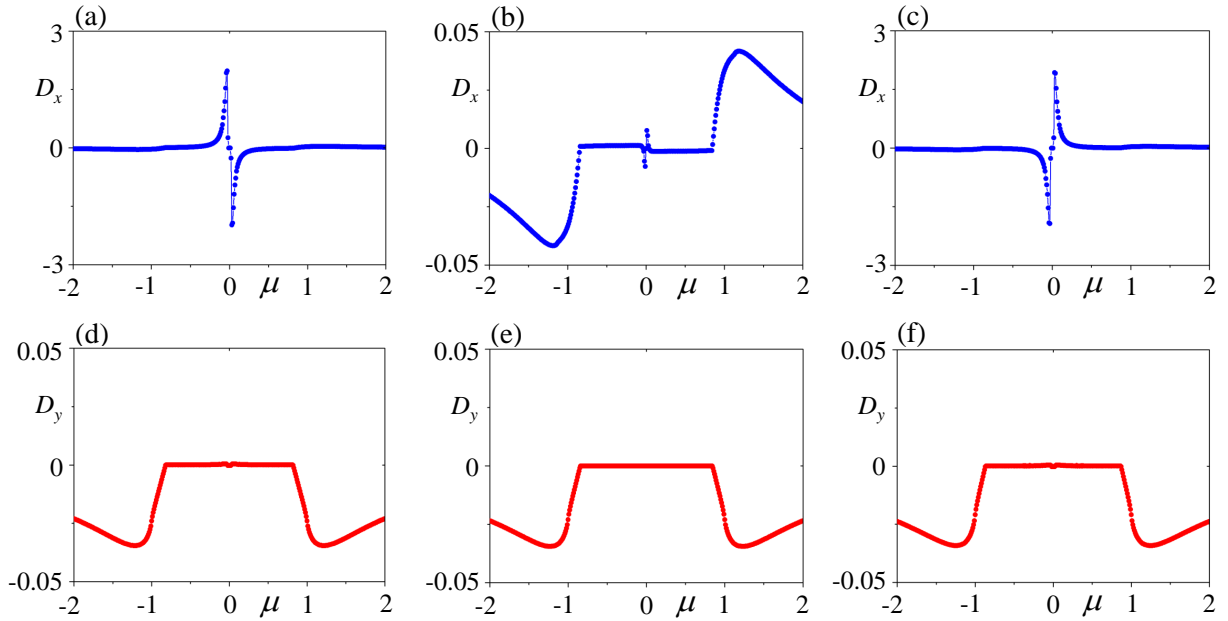


FIG. 3. (Color online) The evolution of D_x and D_y across the critical point at $m = 1$. Common parameters are $t_0 = 0$, $t_1 = t_3 = 1$ and $t_2 = t_4 = 2$. $m = 0.95$ in (a)(d), $m = 1$ in (b)(e), and $m = 1.05$ in (c)(f).

the Dirac cones which describes the low-energy physics. To see this, we consider $m \rightarrow 1$, so that the low-energy physics is described by the Dirac Hamiltonians at $\mathbf{K}_{\pm} = (\pi, \pm\pi/2)$. By expanding the Hamiltonian in Eq.(7) around \mathbf{K}_{\pm} to the linear order in momentum, the Dirac Hamiltonians have the form

$$H_{\mathbf{K}_{\pm}}(\mathbf{q}) = \mp t_0 q_x \mp t_1 q_y \sigma_x - t_2 q_x \sigma_y + \tilde{m} \sigma_z, \quad (9)$$

where $\tilde{m} = m - t_3$ and \mathbf{q} represents the momentum measured from \mathbf{K}_+ or \mathbf{K}_- . It becomes apparent that the t_0 term tilts the two Dirac cones along the x direction in an opposite way. Restricting to the low-energy Hamiltonians, the Berry curvatures around \mathbf{K}_{\pm} have the form

$$\begin{aligned} \Omega_{\mathbf{K}_+}^{(\pm)}(\mathbf{q}) &= \mp \frac{t_1 t_2 \tilde{m}}{2(t_1^2 q_y^2 + t_2^2 q_x^2 + \tilde{m}^2)^{3/2}}, \\ \Omega_{\mathbf{K}_-}^{(\pm)}(\mathbf{q}) &= \pm \frac{t_1 t_2 \tilde{m}}{2(t_1^2 q_y^2 + t_2^2 q_x^2 + \tilde{m}^2)^{3/2}}. \end{aligned} \quad (10)$$

One can find the Berry curvatures are even under $q_y \rightarrow -q_y$. Because the Fermi-Dirac distribution function is also even under $q_y \rightarrow -q_y$, it can be readily inferred from Eq.(6) that D_y will vanish if restricting to the above linear Dirac Hamiltonians. This analysis suggests that if D_y is nonzero for the full Hamiltonian, the nonzero parts come from higher-order contributions and thus should be small when the system is close to the critical point and the chemical potential is located near the band edge.

Depending on the extent of tilt, the Dirac cones are commonly classified as type-I and type-II ones. For this model, as the tilt only affects the result quantitatively, we will focus on

type-I Dirac cones, i.e. $|t_0| < |t_2|$, so that the Hamiltonian describes a true insulator when the chemical potential is located within the gap of Dirac cones. In Fig.3, we show the evolution of D_x and D_y across the critical point at $m = 1$ for a broad range of doping levels. From Figs.3(a)-(c), it is readily seen that D_x dramatically changes its sign when the system crosses the critical point. Furthermore, on both sides, D_x takes a very large value when the chemical potential is located near the band edge. In contrast, from Figs.3(d)-(f), one can find that D_y does not display any dramatic change and is vanishingly small when the doping level is lower than a threshold, agreeing with the previous analysis based on the low-energy linear Dirac Hamiltonians.

The dramatic sign change of D_x across the critical point can be understood from Eq.(10). Since the Dirac mass \tilde{m} changes sign when the system crosses the critical point, one can infer from Eq.(10) that the Berry curvatures at \mathbf{K}_{\pm} switch their sign. As the locations of the two Dirac cones are fixed in momentum space, the sign change in Berry curvatures directly leads to the sign change of D_x . On the other hand, the large value of D_x near the band edge is a consequence of the large Berry curvature, the large density of states and the tilt which makes the Fermi velocity finite at the band edge.

B. Insulators with low-energy semi-Dirac cones

For the first model, the low-energy physics near the phase boundary is captured by linear Dirac cones. In this section, we replace the linear Dirac cones by semi-Dirac cones whose dispersions are quadratic in one direction and linear in other

directions when the Dirac mass vanishes. To realize such semi-Dirac cones, we substitute the DPs by semi-Dirac points (SDP) which correspond to the mergence of two Dirac points with opposite winding numbers. To be specific, we consider that d_i have the form

$$\begin{aligned} d_0(\mathbf{k}) &= 0, & d_x(\mathbf{k}) &= t_1 \sin k_x \sin k_y, \\ d_y(\mathbf{k}) &= t_2 \sin k_x + t_3 \sin k_y, \\ d_z(\mathbf{k}) &= (m + t_4 \cos k_x + t_5 \cos k_y). \end{aligned} \quad (11)$$

Here we set $d_0(\mathbf{k}) = 0$ because the Hamiltonian does not have any crystalline symmetry even when the d_0 term is absent. In addition, here as the SDPs satisfying $d_x(\mathbf{k}) = d_y(\mathbf{k}) = 0$ are fixed at time-reversal invariant momentum, one cannot add a term to tilt the linear direction while preserving the time-reversal symmetry. Although the SDPs correspond to a critical situation and they can be gapped by an arbitrary small time-reversal symmetric perturbation of the form $\delta\sigma_x$, one can view two nearby DPs with opposite winding numbers as an effective SDP and the above Hamiltonian can be applied to describe such more realistic situations.

In the first model, we have shown that the relative configuration between BIS and DPs determines whether the system falls into the obstructed regime or the trivial regime. Without the loss of generality, we take $t_{1,2,3,4,5} = 1$ for a concrete discussion in the following. For this set of parameters, the BIS encloses the SDP at the $\Gamma = (0, 0)$ point when $-2 < m < 0$ and encloses the SDP at the $\mathbf{M} = (\pi, \pi)$ point when $0 < m < 2$. At $m = \pm 2$ and $m = 0$, the BIS crosses one and two SDPs, respectively, leading to the closing of bulk gap. According to the analysis, if we make a similar assumption as the previous case that the SDPs are fixed there, then $0 < |m| < 2$ corresponds to the obstructed regime and $|m| > 2$ corresponds to the trivial regime.

In Fig.4, the energy spectra for a cylinder geometry as well as the hybrid Wannier centers are shown. Because the Hamiltonian does not change under the exchange $k_x \rightarrow k_y$ for the chosen set of parameters, the results shown in Fig.4 does not change if k_x is substituted by k_y , so here we only show one of them to avoid repetition. The results for $m = 1.5$ are shown in Figs.4(a)(c). One can find that the open edges harbor mid-gap states, and the hybrid Wannier centers cross the domain boundary $\nu = 0.5$ at $k_x = \pi$. In contrast, when $m = 2.5$, which falls into the trivial regime, one can find from Figs.4(b)(d) that the open edges do not harbor any mid-gap state, and the hybrid Wannier centers instead only cross the domain center $\nu = 0$ at both $k_x = 0$ and $k_x = \pi$.

Now we investigate the evolution of D_x and D_y across the critical points. Without the loss of generality, we focus on the critical point at $m = 2$. Near this critical point, the band edge is located at $\mathbf{M} = (\pi, \pi)$, so we do a low-energy expansion around this point. For simplicity, we only keep the leading-order term for each of the d_i components. As a result, the low-energy Hamiltonian reads

$$H_M(\mathbf{q}) = t_1 q_x q_y \sigma_x - (t_2 q_x + t_3 q_y) \sigma_y + \tilde{m} \sigma_z. \quad (12)$$

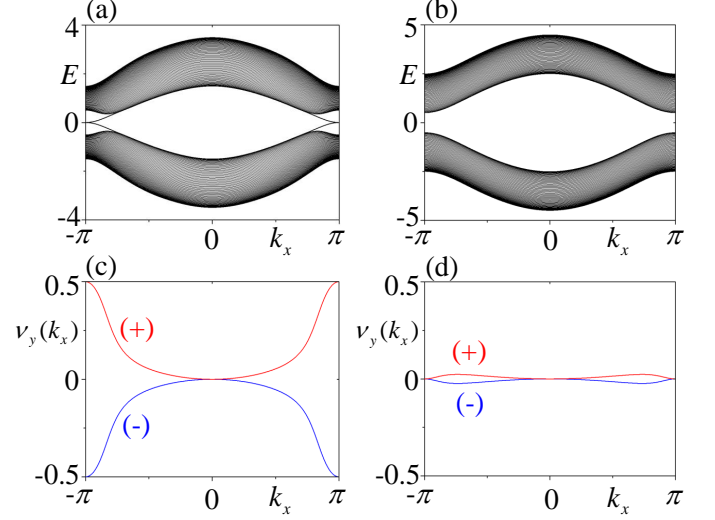


FIG. 4. (Color online) (a)(b) show the energy spectra under a cylinder geometry with open boundary conditions in the y direction and periodic boundary conditions in the x direction. (c)(d) show the hybrid Wannier centers $\nu_y^{(\pm)}(k_x)$. Common parameters are $t_1 = t_2 = t_3 = t_4 = t_5 = 1$. $m = 1.5$ in (a)(c), and $m = 2.5$ in (b)(d).

Here $\tilde{m} = m - t_4 - t_5$ and \mathbf{q} represents the momentum measured from \mathbf{M} . At $\tilde{m} = 0$, the dispersion of this Hamiltonian is quadratic in the direction satisfying $t_2 q_x + t_3 q_y = 0$. The Berry curvatures for this low-energy Hamiltonian read

$$\Omega_M^{(\pm)}(\mathbf{q}) = \pm \frac{t_1(t_2 q_x - t_3 q_y) \tilde{m}}{2 [t_1^2 q_x^2 q_y^2 + (t_2 q_x + t_3 q_y)^2 + \tilde{m}^2]^{3/2}}. \quad (13)$$

The Berry curvatures have two interesting properties. One is still the sign change when the system crosses the critical point. The second one is that the Berry curvature is odd under the exchange $q_x \leftrightarrow q_y$ when $t_2 = t_3$. The second property can be simply inferred from the definition of Berry curvature which is antisymmetric about the two orthogonal momenta in two dimensions (see Eq.(3)).

The evolutions of D_x and D_y crossing the critical point $m = 2$ are shown in Fig.5. The results indicate that D_x and D_y will dramatically change their signs when the system crosses the critical point. In addition, one can find that $D_x = -D_y$ is always hold for the given parameters, regardless of the doping level. These two main features can be explained by the two properties of Berry curvatures discussed above.

Compared to Fig.3, one can find that when the doping level is near the band edge, D_x in Fig.5 is much smaller. This remarkable difference can be understood through the difference in their Berry curvatures. According to Eq.(10), the Berry curvatures for the linear Dirac cones are peaked at $\mathbf{q} = 0$ with a height proportional to $1/2\tilde{m}^2$. In contrast, according to Eq.(13), the Berry curvature for the semi-Dirac cone is linear in momentum [48], and thus vanish in the limit $\mathbf{q} \rightarrow 0$ when \tilde{m} is still finite.

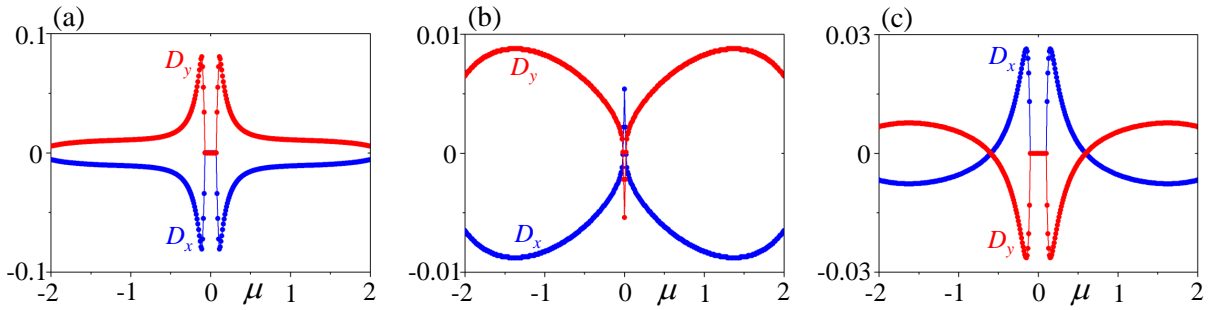


FIG. 5. (Color online) The evolution of D_x and D_y across the critical point at $m = 2$. Common parameters are $t_1 = t_2 = t_3 = t_4 = t_5 = 1$. $m = 1.9$ in (a), $m = 2$ in (b), and $m = 2.1$ in (c). $D_x = -D_y$ in (a)-(c).

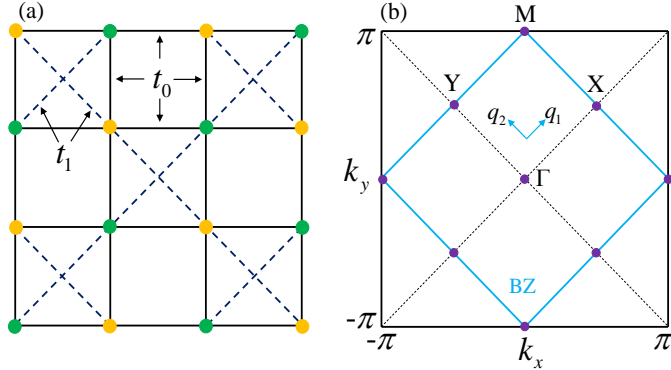


FIG. 6. (Color online) (a) A schematic diagram of the lattice and hoppings. t_0 denotes the nearest neighbor hopping, and t_1 denotes the next-nearest neighbor hopping. The yellow and green dots denote two kinds of sublattice. (b) The cyan square is the first Brillouin zone of the lattice in (a).

IV. Nonlinear Hall effect in doped class AI semimetals

By far the two studied models have gapped band structure and the locations of linear or semi-Dirac cones are fixed. As semimetals are also of great interest, below we consider a simple two-band model which has gapless band structure in

a broad regime. To be specific, we consider the staggered Mielke model whose real-space hoppings and first Brillouin zone are illustrated in Figs.6(a) and (b), respectively. For this model, the four components of d_i take the form [52, 53]

$$\begin{aligned} d_0(\mathbf{k}) &= 2t_1 \cos k_x \cos k_y, \\ d_x(\mathbf{k}) &= 2t_0(\cos k_x + \cos k_y) \cos k_y, \\ d_y(\mathbf{k}) &= 2t_0(\cos k_x + \cos k_y) \sin k_y, \\ d_z(\mathbf{k}) &= 2t_1 \sin k_x \sin k_y + \delta. \end{aligned} \quad (14)$$

This Hamiltonian has quite a few salient features. First, it is the simplest model which can realize a flat band with non-trivial geometrical and topological properties. Second, while this Hamiltonian does not have inversion symmetry, the existence of a glide symmetry allows the band structure to have stable band degeneracies at the Brillouin zone boundary when the on-site offset potential δ is smaller than twice the diagonal hopping t_1 , i.e. $|\delta| < 2|t_1|$. Third, with the variation of δ , the topological properties of the band degeneracies will change, and the band degeneracies will move in momentum space, merge when $|\delta| = 2|t_1|$, and then annihilate and disappear when $|\delta| > 2|t_1|$.

To see how the topological properties as well as the locations of band degeneracies evolve with respect to δ , we write down the energy spectra explicitly, which read

$$E_{\pm}(\mathbf{k}) = 2t_1 \cos k_x \cos k_y \pm \sqrt{(2t_1 \sin k_x \sin k_y + \delta)^2 + 4t_0^2(\cos k_x + \cos k_y)^2}. \quad (15)$$

It is easy to see that, depending on the sign of δ , the band degeneracies are forced to appear either on the line $k_y = k_x + \pi$ or on the line $k_y = -k_x + \pi$. Without the loss of generality, below we take $t_0 = t_1 = 0.5$ and focus on $\delta \geq 0$ for a concrete discussion. For this set of parameters, one can find that the band degeneracies are located at two inequivalent momenta, $\mathbf{Q}_1 = (-\arcsin \sqrt{\delta}, -\arcsin \sqrt{\delta} + \pi)$ and $\mathbf{Q}_2 = (-\pi + \arcsin \sqrt{\delta}, \arcsin \sqrt{\delta})$. Furthermore, the band

degeneracies are located at the energy $E = \delta - 1$ when $0 \leq \delta \leq 1$. Two limits are of special interest. One limit is at $\delta = 0$. When $\delta = 0$, \mathbf{Q}_1 and \mathbf{Q}_2 are equivalent up to a reciprocal lattice vector. By expanding the Hamiltonian around $(0, \pi)$, the low-energy Hamiltonian up to the second order in momentum takes the form

$$H_{(0, \pi)}(\mathbf{q}) = -1 + \frac{q^2}{2} - q_x q_y \sigma_z + \frac{1}{2}(q_x^2 - q_y^2) \sigma_x, \quad (16)$$

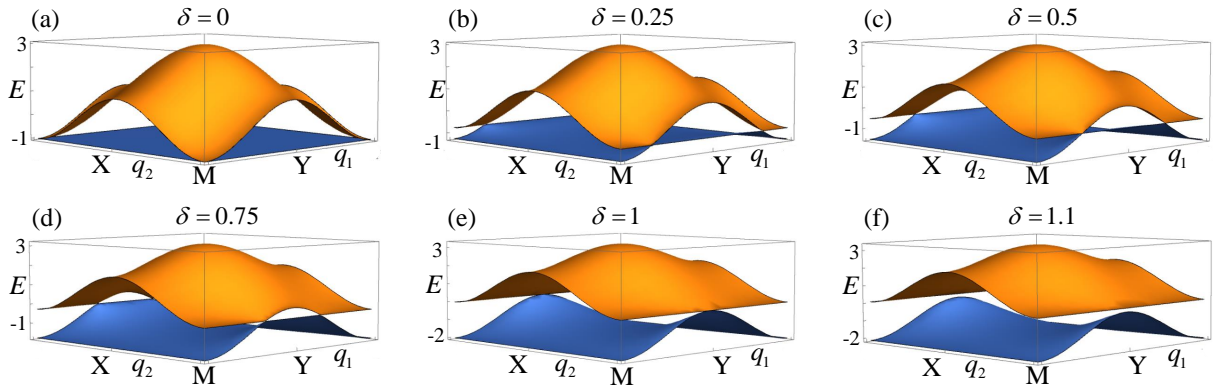


FIG. 7. (Color online) Bulk energy spectra of the Mielke model. Common parameters are $t_0 = t_1 = 0.5$. (a) $\delta = 0$, (b) $\delta = 0.25$, (c) $\delta = 0.5$, (d) $\delta = 0.75$, (e) $\delta = 1$ and (f) $\delta = 1.1$.

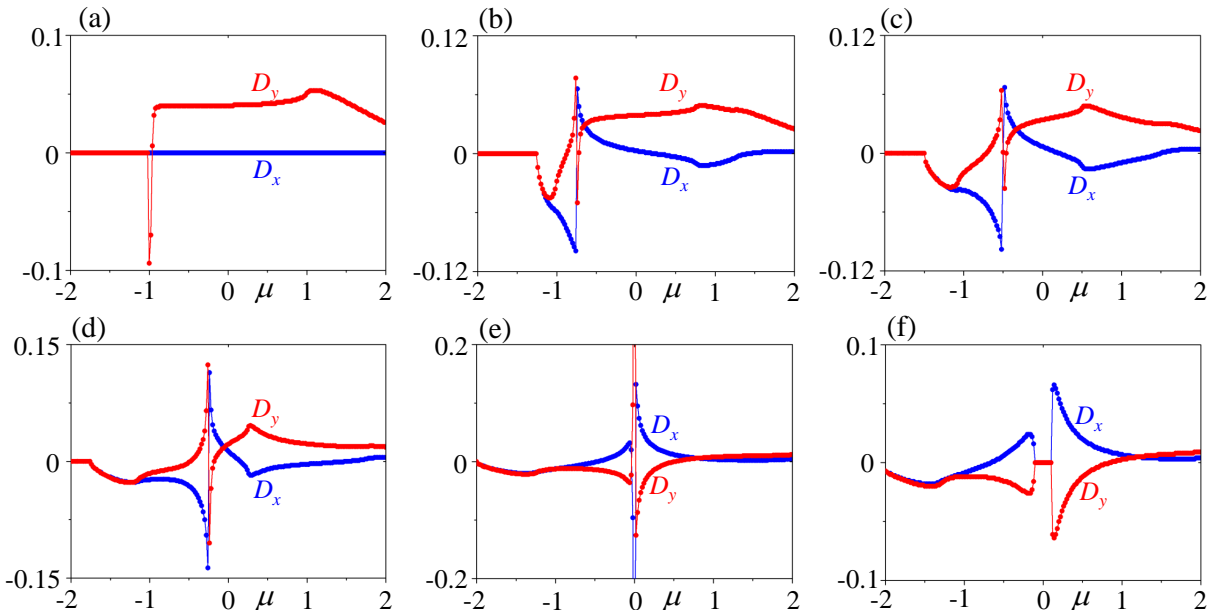


FIG. 8. (Color online) The evolutions of D_x and D_y with respect to the movement and annihilation of DPs. Common parameters are $t_0 = t_1 = 0.5$. (a) $\delta = 0$, (b) $\delta = 0.25$, (c) $\delta = 0.5$, (d) $\delta = 0.75$, (e) $\delta = 1$ and (f) $\delta = 1.1$.

where $q^2 = q_x^2 + q_y^2$. According to this low-energy Hamiltonian, one can find that the dispersions of the two bands follow $E_-(\mathbf{q}) = -1$ and $E_+(\mathbf{q}) = -1 + q^2$, which indicates that the upper dispersive band touches quadratically with the lower flat band at $(0, \pi)$. The quadratical touching point has winding number ± 2 ($+2$ or -2 depends on the detail of definition), which can be viewed as the mergence of two DPs with the same winding number ± 1 . The other limit is at $\delta = 1$. When $\delta = 1$, the two band degeneracies merge again at $\mathbf{Y} = (-\pi/2, \pi/2)$. By expanding the Hamiltonian around \mathbf{Y} , however, one will find that the low-energy Hamiltonian up to the second order in momentum takes the form

$$H_{\mathbf{Y}}(\mathbf{q}) = -q_x q_y + \frac{q^2}{2} \sigma_z + (q_x - q_y) \sigma_y. \quad (17)$$

The energy dispersion is quadratic only in the direction $q_x = q_y$. This band degeneracy has zero winding number and corresponds to a SDP discussed previously. It may look counterintuitive at first sight that the winding number is not conserved when δ is varied from 0 to 1. However, it is worth noting that the winding number is only well-defined for the low-energy Hamiltonian which has an emerging chiral symmetry when $\delta \leq 1$ and neglecting the d_0 term which does not affect the geometrical properties of the Bloch wave functions. The full Hamiltonian itself does not have the chiral symmetry. In addition, even for the low-energy Hamiltonian, its chiral operator C , which satisfies $\{C, H(\mathbf{q})\} = 0$, is not fixed. Instead, it evolves from $C = \sigma_y$ to $C = \sigma_x$ when δ is varied from 0 to 1 (a more thorough discussion about this can be found in

Ref.[53]). For this two-band Hamiltonian, the winding number counts the number of times that the vector composed by the remaining components of $\{d_x, d_y, d_z\}$ rotates around the axis characterized by the chiral operator when the momentum changes in a closed path encircling the band degeneracy. As the chiral operator changes, the non-conservation of winding number is similar to the angular momentum, which is also not conserved if the rotation symmetry axis is changed.

More details about how the band structure changes with respect to δ are provided in Fig.7. From Fig.7(a), one can see that when $\delta = 0$, the lower band is completely flat and the upper dispersive band touches it quadratically at the corner of the first Brillouin zone. When δ becomes nonzero, the lower band also becomes dispersive, but it remains flat along the line **M-X**. From Figs.7(b)-(d), one can find that, within the regime $0 < \delta < 1$, the two bands touch at two inequivalent momenta and form two DPs on the line **M-Y**. It is worth noting that, in this regime, the tilt of the linear Dirac cones falls into the critical situation which corresponds to the boundary between type-I and type-II Dirac cones. For linear Dirac cones with such a critical tilt, they are commonly dubbed as type-III Dirac cones for differentiation. From Fig.7(e), one can see that when $\delta = 1$, the two DPs merge at **Y** and form a SDP. Here the SDP is a critical point which separates the semimetal phase from the insulator phase. When $\delta > 1$, the two bands are separated, and the upper band becomes flat along the line **M-Y**, as shown in Fig.7(f).

Now let us investigate how D_x and D_y respond to the change of band structure. Fig.8(a) shows the result for $\delta = 0$. For this case, we find that D_x vanishes identically, which is due to the accidental mirror symmetry \mathcal{M}_y at this limit. In contrast, D_y has a dramatic change when the chemical potential crosses $\mu = -1$. As the quadratical touching point is located at $E = -1$ when $\delta = 0$, the dramatic change in D_y at $\mu = -1$ corresponds to that the doping level meets the quadratical touching point at which the Berry curvature is divergent. As a finite δ breaks the mirror symmetry \mathcal{M}_y , D_x also becomes finite when the chemical potential crosses the bands. Most remarkably, from Figs.8(b)-(d), we find that, when $0 < \delta < 1$, D_x and D_y simultaneously undergo a dramatic change when the doping level sweeps $\mu = -1 + \delta$. We have discussed previously that the DPs are located at $E = -1 + \delta$ when $0 < \delta < 1$, so the reason for the dramatic change is also that the doping level meets the DPs at which the Berry curvature is divergent. When the DPs merge together at $\delta = 1$, D_x and D_y undergo a dramatic change at $\mu = 0$ as expected, but with their peak values greatly enhanced, as shown in Fig.8(e). When $\delta > 1$, both D_x and D_y vanish when the doping level is located within the bulk gap, and their peak values are located near the band edge, as shown in Fig.8(f). Because the two bands are not symmetric about $E = 0$ due to the existence of the d_0 term, D_x and D_y are also not symmetric about $\mu = 0$.

V. DISCUSSION AND CONCLUSION

Although the class AI does not host strong topological insulator phase in two dimensions, we have shown that the band structures of inversion asymmetric insulators and semimetals belonging to this class can have nontrivial geometrical and topological properties. For insulators close to the critical points, we find that the low-energy physics is described by either linear Dirac Hamiltonians or semi-Dirac Hamiltonians. For both kinds of Hamiltonians, the local Berry curvature near the band edge will become more prominent with the decrease of Dirac mass, and will change sign when the system crosses the critical point. Interestingly, we find that the BCD follows the same behavior as the Berry curvature, indicating that the nonlinear Hall effect can reflect the change in local quantum geometry as well as the global topology of the band structures in such materials. For the semimetals, in this work we have investigated the Mielke model. For this model, the distribution of the local Berry curvature and the topological properties of the band degeneracies will change with the movement of DPs in momentum space. As the local Berry curvature is divergent at the DPs and the density of states is nonzero for energy at which the type-III DPs are located, we find that the BCDs also become more and more prominent when the doping level is tuned more and more close to the DPs. In addition, as the Berry curvatures of conduction and valence bands have opposite signs, we find that the BCDs sharply reverse their signs when the doping level is tuned across the DPs. As two dimensional materials have advantage in tuning the doping level, this remarkable sensitivity of nonlinear Hall effect to the chemical potential near the DPs may have interesting applications in optoelectronics, like sensors, and can also be applied to determine the locations of DPs in real materials as a complementary method of angle-resolved photoemission spectroscopy.

From the three models we have studied, we find that the nonlinear Hall effect can be rather prominent in both doped class AI insulators and semimetals. Our study also reveals that the tilt of gapped or gapless Dirac cones can benefit the enhancement of nonlinear Hall effect near the band edge. This enhancement can be understood by noting that the BCD is co-determined by the density of states, Fermi velocity and Berry curvature on the Fermi surface. For upright gapped Dirac cones, because the density of states and the Berry curvature are finite and the Fermi velocity vanishes at the band edge, the BCD will accordingly vanish when the doping level is exactly located at the band edge. For upright gapless Dirac cones, while the Berry curvature is divergent and the Fermi velocity is finite, the density of states vanishes when the Fermi level is exactly located at the DPs, also leading a zero BCD. Without affecting the Berry curvature, a finite tilt of gapped Dirac cones can make the Fermi velocity at the band edge finite, and a sufficient strong tilt of gapless Dirac cones can make the density of states nonzero even though the Fermi level is exactly located at the DPs, consequently leading to the enhancement.

Similar to the linear anomalous Hall effect, nonlinear Hall effect in fact can also have contributions from disorder-induced side jump and skew scattering [57–62]. However, In this work we have restricted ourselves to the intrinsic part. We will leave the investigation of the disorder-induced contributions in this class of materials for future work. Overall, from a low-energy perspective, the three models we have studied are quite representative in the description of class AI materials without inversion symmetry. As the class AI requires the spin-orbit coupling to be negligible, our findings in this work are relevant to materials consisting of only light elements. Among various possibilities, we suggest the application of organic materials to test our predictions since very recently the experimental observation of nonlinear Hall effect in such materials has been reported [63].

VI. ACKNOWLEDGEMENTS

Z.S.L. and H.H.Z. are supported by the National Natural Science Foundation of China (NSFC) under Grant No. 11875327. Z.Y. is supported by the National Science Foundation of China (Grant No. 11904417) and Z.Y. is supported by the National Natural Science Foundation of China (Grant No. 11904417) and the Natural Science Foundation of Guangdong Province (Grant No. 2021B1515020026).

* yanzhb5@mail.sysu.edu.cn

- [1] Xiao-Liang Qi, Taylor L. Hughes, and Shou-Cheng Zhang, “Topological field theory of time-reversal invariant insulators,” *Phys. Rev. B* **78**, 195424 (2008).
- [2] Naoto Nagaosa, Jairo Sinova, Shigeki Onoda, A. H. MacDonald, and N. P. Ong, “Anomalous hall effect,” *Rev. Mod. Phys.* **82**, 1539–1592 (2010).
- [3] Di Xiao, Ming-Che Chang, and Qian Niu, “Berry phase effects on electronic properties,” *Rev. Mod. Phys.* **82**, 1959–2007 (2010).
- [4] F. D. M. Haldane, “Model for a quantum hall effect without landau levels: Condensed-matter realization of the “parity anomaly”,” *Phys. Rev. Lett.* **61**, 2015–2018 (1988).
- [5] Rui Yu, Wei Zhang, Hai-Jun Zhang, Shou-Cheng Zhang, Xi Dai, and Zhong Fang, “Quantized anomalous hall effect in magnetic topological insulators,” *Science* **329**, 61 (2010).
- [6] Cui-Zu Chang, Jinsong Zhang, Xiao Feng, Jie Shen, Zuocheng Zhang, Minghua Guo, Kang Li, Yunbo Ou, Pang Wei, Li-Li Wang, Zhong-Qing Ji, Yang Feng, Shuaihua Ji, Xi Chen, Jinfeng Jia, Xi Dai, Zhong Fang, Shou-Cheng Zhang, Ke He, Yanyu Wang, Li Lu, Xu-Cun Ma, and Qi-Kun Xue, “Experimental observation of the quantum anomalous hall effect in a magnetic topological insulator,” *Science* **340**, 167–170 (2013), <https://science.sciencemag.org/content/340/6129/167.full.pdf>.
- [7] Klaus von Klitzing, “Essay: Quantum hall effect and the new international system of units,” *Phys. Rev. Lett.* **122**, 200001 (2019).
- [8] J. E. Sipe and A. I. Shkrebtii, “Second-order optical response in semiconductors,” *Phys. Rev. B* **61**, 5337–5352 (2000).
- [9] Pavan Hosur, “Circular photogalvanic effect on topological insulator surfaces: Berry-curvature-dependent response,” *Phys. Rev. B* **83**, 035309 (2011).
- [10] Fernando de Juan, Adolfo G. Grushin, Takahiro Morimoto, and Joel E. Moore, “Quantized circular photogalvanic effect in weyl semimetals,” *Nature Communications* **8**, 15995 (2017).
- [11] Liang Z. Tan and Andrew M. Rappe, “Enhancement of the bulk photovoltaic effect in topological insulators,” *Phys. Rev. Lett.* **116**, 237402 (2016).
- [12] Ashley M. Cook, Benjamin M. Fregoso, Fernando de Juan, Siniša Coh, and Joel E. Moore, “Design principles for shift current photovoltaics,” *Nature Communications* **8**, 14176 (2017).
- [13] Xu Yang, Kenneth Burch, and Ying Ran, “Divergent bulk photovoltaic effect in Weyl semimetals,” *arXiv e-prints*, arXiv:1712.09363 (2017), arXiv:1712.09363 [cond-mat.mes-hall].
- [14] Zhongbo Yan, “Precise determination of critical points of topological phase transitions via shift current in two-dimensional inversion asymmetric insulators,” *arXiv e-prints*, arXiv:1812.02191 (2018), arXiv:1812.02191 [cond-mat.mes-hall].
- [15] Gavin B. Osterhoudt, Laura K. Diebel, Mason J. Gray, Xu Yang, John Stanco, Xiangwei Huang, Bing Shen, Ni Ni, Philip J. W. Moll, Ying Ran, and Kenneth S. Burch, “Colossal mid-infrared bulk photovoltaic effect in a type-i weyl semimetal,” *Nature Materials* **18**, 471–475 (2019).
- [16] J. E. Moore and J. Orenstein, “Confinement-induced berry phase and helicity-dependent photocurrents,” *Phys. Rev. Lett.* **105**, 026805 (2010).
- [17] Inti Sodemann and Liang Fu, “Quantum nonlinear hall effect induced by berry curvature dipole in time-reversal invariant materials,” *Phys. Rev. Lett.* **115**, 216806 (2015).
- [18] Takahiro Morimoto and Naoto Nagaosa, “Topological nature of nonlinear optical effects in solids,” *Science Advances* **2** (2016), 10.1126/sciadv.1501524, <https://advances.sciencemag.org/content/2/5/e1501524.full.pdf>.
- [19] Junyeong Ahn, Guang-Yu Guo, and Naoto Nagaosa, “Low-frequency divergence and quantum geometry of the bulk photovoltaic effect in topological semimetals,” *Phys. Rev. X* **10**, 041041 (2020).
- [20] Hikaru Watanabe and Youichi Yanase, “Chiral photocurrent in parity-violating magnet and enhanced response in topological antiferromagnet,” *Phys. Rev. X* **11**, 011001 (2021).
- [21] Yang Zhang, Yan Sun, and Binghai Yan, “Berry curvature dipole in weyl semimetal materials: An ab initio study,” *Phys. Rev. B* **97**, 041101 (2018).
- [22] Habib Rostami and Marco Polini, “Nonlinear anomalous photocurrents in weyl semimetals,” *Phys. Rev. B* **97**, 195151 (2018).
- [23] Cheng Chen, Huaiqiang Wang, Dinghui Wang, and Haijun Zhang, “Strain-engineered nonlinear hall effect in hgte,” *SPIN* **09**, 1940017 (2019).
- [24] O. Matsyshyn and I. Sodemann, “Nonlinear hall acceleration and the quantum rectification sum rule,” *Phys. Rev. Lett.* **123**, 246602 (2019).
- [25] Habib Rostami and Vladimir Jurićić, “Probing quantum criticality using nonlinear hall effect in a metallic dirac system,” *Phys. Rev. Research* **2**, 013069 (2020).
- [26] Yang Gao, Furu Zhang, and Wei Zhang, “Second-order nonlinear hall effect in weyl semimetals,” *Phys. Rev. B* **102**, 245116 (2020).
- [27] Sobhit Singh, Jinwoong Kim, Karin M. Rabe, and David Vanderbilt, “Engineering weyl phases and nonlinear hall effects in t_d -mote₂,” *Phys. Rev. Lett.* **125**, 046402 (2020).

[28] Sami Dzsaber, Xinlin Yan, Mathieu Taupin, Gaku Eguchi, Andrey Prokofiev, Toni Shiroka, Peter Blaha, Oleg Rubel, Sarah E. Grefe, Hsin-Hua Lai, Qimiao Si, and Silke Paschen, “Giant spontaneous hall effect in a nonmagnetic weyl-kondo semimetal,” *Proceedings of the National Academy of Sciences* **118** (2021), 10.1073/pnas.2013386118, <https://www.pnas.org/content/118/8/e2013386118.full.pdf>.

[29] Chuanchang Zeng, Snehasish Nandy, and Sumanta Tewari, “Berry curvature dipole in topological Weyl semimetals,” arXiv e-prints, arXiv:2009.05043 (2020), arXiv:2009.05043 [cond-mat.mes-hall].

[30] Dushyant Kumar, Chuang-Han Hsu, Raghav Sharma, Tay-Rong Chang, Peng Yu, Junyong Wang, Goki Eda, Gengchiah Liang, and Hyunsoo Yang, “Room-temperature nonlinear hall effect and wireless radiofrequency rectification in weyl semimetal tairte4,” *Nature Nanotechnology* (2021), 10.1038/s41565-020-00839-3.

[31] Su-Yang Xu, Qiong Ma, Huitao Shen, Valla Fatemi, Sanfeng Wu, Tay-Rong Chang, Guoqing Chang, Andrés M. Mier Valdivia, Ching-Kit Chan, Quinn D. Gibson, Jiadong Zhou, Zheng Liu, Kenji Watanabe, Takashi Taniguchi, Hsin Lin, Robert J. Cava, Liang Fu, Nuh Gedik, and Pablo Jarillo-Herrero, “Electrically switchable berry curvature dipole in the monolayer topological insulator wte2,” *Nature Physics* **14**, 900–906 (2018).

[32] Qiong Ma, Su-Yang Xu, Huitao Shen, David MacNeill, Valla Fatemi, Tay-Rong Chang, Andrés M. Mier Valdivia, Sanfeng Wu, Zongzheng Du, Chuang-Han Hsu, Shiang Fang, Quinn D. Gibson, Kenji Watanabe, Takashi Taniguchi, Robert J. Cava, Efthimios Kaxiras, Hai-Zhou Lu, Hsin Lin, Liang Fu, Nuh Gedik, and Pablo Jarillo-Herrero, “Observation of the nonlinear hall effect under time-reversal-symmetric conditions,” *Nature* **565**, 337–342 (2019).

[33] Kaifei Kang, Tingxin Li, Egon Sohn, Jie Shan, and Kin Fai Mak, “Nonlinear anomalous hall effect in few-layer wte2,” *Nature Materials* **18**, 324–328 (2019).

[34] Z. Z. Du, C. M. Wang, Hai-Zhou Lu, and X. C. Xie, “Band signatures for strong nonlinear hall effect in bilayer wte₂,” *Phys. Rev. Lett.* **121**, 266601 (2018).

[35] Jhih-Shih You, Shiang Fang, Su-Yang Xu, Efthimios Kaxiras, and Tony Low, “Berry curvature dipole current in the transition metal dichalcogenides family,” *Phys. Rev. B* **98**, 121109 (2018).

[36] Yang Zhang, Jeroen van den Brink, Claudia Felser, and Binghai Yan, “Electrically tuneable nonlinear anomalous hall effect in two-dimensional transition-metal dichalcogenides WTe₂ and MoTe₂,” *2D Materials* **5**, 044001 (2018).

[37] Hua Wang and Xiaofeng Qian, “Ferroelectric nonlinear anomalous hall effect in few-layer wte2,” *npj Computational Materials* **5**, 119 (2019).

[38] Rui-Chun Xiao, Ding-Fu Shao, Zhi-Qiang Zhang, and Hua Jiang, “Two-dimensional metals for piezoelectriclike devices based on berry-curvature dipole,” *Phys. Rev. Applied* **13**, 044014 (2020).

[39] Benjamin T. Zhou, Cheng-Ping Zhang, and K.T. Law, “Highly tunable nonlinear hall effects induced by spin-orbit couplings in strained polar transition-metal dichalcogenides,” *Phys. Rev. Applied* **13**, 024053 (2020).

[40] Jin-Xin Hu, Cheng-Ping Zhang, Ying-Ming Xie, and K. T. Law, “Nonlinear Hall Effects in Strained Twisted Bilayer WSe₂,” arXiv e-prints, arXiv:2004.14140 (2020), arXiv:2004.14140 [cond-mat.mes-hall].

[41] Meizhen Huang, Zefei Wu, Jinxin Hu, Xiangbin Cai, En Li, Li-heng An, Xuemeng Feng, Ziqing Ye, Nian Lin, Kam Tuen Law, and Ning Wang, “Giant nonlinear Hall effect in twisted WSe₂,” arXiv e-prints, arXiv:2006.05615 (2020), arXiv:2006.05615 [cond-mat.mes-hall].

[42] Raffaele Battilomo, Niccoló Scopigno, and Carmine Ortix, “Berry curvature dipole in strained graphene: A fermi surface warping effect,” *Phys. Rev. Lett.* **123**, 196403 (2019).

[43] Cheng-Ping Zhang, Jiewen Xiao, Benjamin T. Zhou, Jin-Xin Hu, Ying-Ming Xie, Binghai Yan, and K. T. Law, “Giant nonlinear Hall effect in strained twisted bilayer graphene,” arXiv e-prints, arXiv:2010.08333 (2020), arXiv:2010.08333 [cond-mat.mes-hall].

[44] Pierre A. Pantaleon, Tony Low, and Francisco Guinea, “Tunable large Berry dipole in strained twisted bilayer graphene,” arXiv e-prints, arXiv:2010.11086 (2020), arXiv:2010.11086 [cond-mat.mes-hall].

[45] Jorge I. Facio, Dmitri Efremov, Klaus Koepernik, Jhih-Shih You, Inti Sodemann, and Jeroen van den Brink, “Strongly enhanced berry dipole at topological phase transitions in btei,” *Phys. Rev. Lett.* **121**, 246403 (2018).

[46] Carmine Ortix, “Nonlinear Hall effect with time-reversal symmetry: Theory and material realizations,” arXiv e-prints, arXiv:2104.06690 (2021), arXiv:2104.06690 [cond-mat.mes-hall].

[47] Qiong Ma, Adolfo G. Grushin, and Kenneth S. Burch, “Topology and geometry under the nonlinear electromagnetic spotlight,” arXiv e-prints, arXiv:2103.03269 (2021), arXiv:2103.03269 [cond-mat.mtrl-sci].

[48] Sai Satyam Samal, S. Nandy, and Kush Saha, “Nonlinear transport without spin-orbit coupling or warping in two-dimensional Dirac semimetals,” arXiv e-prints, arXiv:2007.07274 (2020), arXiv:2007.07274 [cond-mat.mes-hall].

[49] Andreas P. Schnyder, Shinsei Ryu, Akira Furusaki, and Andreas W. W. Ludwig, “Classification of topological insulators and superconductors in three spatial dimensions,” *Phys. Rev. B* **78**, 195125 (2008).

[50] Alexei Kitaev, “Periodic table for topological insulators and superconductors,” *AIP conference proceedings*, **1134**, 22–30 (2009).

[51] Shinsei Ryu, Andreas P Schnyder, Akira Furusaki, and Andreas W W Ludwig, “Topological insulators and superconductors: tenfold way and dimensional hierarchy,” *New Journal of Physics* **12**, 065010 (2010).

[52] A Mielke, “Ferromagnetism in the hubbard model on line graphs and further considerations,” *Journal of Physics A: Mathematical and General* **24**, 3311–3321 (1991).

[53] Gilles Montambaux, Lih-King Lim, Jean-Noël Fuchs, and Frédéric Piéchon, “Winding vector: How to annihilate two dirac points with the same charge,” *Phys. Rev. Lett.* **121**, 256402 (2018).

[54] A. H. Castro Neto, F. Guinea, N. M. R. Peres, K. S. Novoselov, and A. K. Geim, “The electronic properties of graphene,” *Rev. Mod. Phys.* **81**, 109–162 (2009).

[55] Xiao-Liang Qi, Yong-Shi Wu, and Shou-Cheng Zhang, “Topological quantization of the spin hall effect in two-dimensional paramagnetic semiconductors,” *Phys. Rev. B* **74**, 085308 (2006).

[56] David Vanderbilt, *Berry Phases in Electronic Structure Theory: Electric Polarization, Orbital Magnetization and Topological Insulators* (Cambridge University Press, 2018).

[57] Z. Z. Du, C. M. Wang, Shuai Li, Hai-Zhou Lu, and X. C. Xie, “Disorder-induced nonlinear hall effect with time-reversal symmetry,” *Nature Communications* **10**, 3047 (2019).

[58] E. J. König, M. Dzero, A. Levchenko, and D. A. Pesin, “Gyrotropic hall effect in berry-curved materials,” *Phys. Rev. B* **99**,

155404 (2019).

[59] Cong Xiao, Z. Z. Du, and Qian Niu, “Theory of nonlinear hall effects: Modified semiclassics from quantum kinetics,” *Phys. Rev. B* **100**, 165422 (2019).

[60] S. Nandy and Inti Sodemann, “Symmetry and quantum kinetics of the nonlinear hall effect,” *Phys. Rev. B* **100**, 195117 (2019).

[61] Hiroki Isobe, Su-Yang Xu, and Liang Fu, “High-frequency rectification via chiral bloch electrons,” *Science Advances* **6** (2020), 10.1126/sciadv.aay2497, <https://advances.sciencemag.org/content/6/13/eaay2497.full.pdf>.

[62] Z. Z. Du, C. M. Wang, Hai-Peng Sun, Hai-Zhou Lu, and X. C. Xie, “Quantum theory of the nonlinear Hall effect,” arXiv e-prints , arXiv:2004.09742 (2020), arXiv:2004.09742 [cond-mat.mes-hall].

[63] Andhika Kiswandhi and Toshihito Osada, “Observation of Nonlinear Anomalous Hall Effect in Organic Two-Dimensional Dirac Fermion System,” arXiv e-prints , arXiv:2103.00300 (2021), arXiv:2103.00300 [cond-mat.str-el].